Phase field fracture in elasto-plastic solids: Numerical implementation and application to transversely isotropic fiber-reinforced composites

Jiajun Zhang[a], Jialu Guo[a], Chencheng Feng[a], Jing Wang[b], Yang Zhang[a,*], A.S. Ademiloye[c,*]

[a]*School of Physics, Nanjing University of Science and Technology, Nanjing 210094, China*
[b]*Key Laboratory of Micro-nano Sensing and IoT of Wenzhou, Wenzhou Institute of Hangzhou Dianzi University, Wenzhou 325038, China*
[c]*Zienkiewicz Institute for Modelling, Data and AI, Faculty of Science and Engineering, Swansea University, Swansea SA1 8EN, United Kingdom*

Abstract

Due to their superior tensile properties, fiber-reinforced composite (FRC) structures have been widely applied in modern industries. This study employs phase field modeling to simulate the process of elastic-plastic fracture in FRC structures. In this study, we first establish a constitutive model for elastoplastic solids and a phase field model for fracture in solid materials. By employing the Newton-Raphson iterative method, the displacement field and phase field are solved separately based on an alternating iterative scheme. Subsequently, we presented three numerical examples to demonstrate the robustness and accuracy of the proposed model. First, we simulated the elastoplastic fracture response of isotropic materials and validate the accuracy of the elastoplastic fracture phase field model. Next, we examined the tensile and fracture behaviors of unidirectional fiber reinforced composite plate with a central circular hole and varying fiber angles. Finally, the influence of curved fiber on the unilateral tensile fracture of FRC plates was investigated. Considering the pronounced heterogeneity between fibers and matrix materials, this study assumes that the fibers remain in the linear elastic regime and introduces a

*Corresponding author
Email addresses: hfutzy@njust.edu.cn (Yang Zhang), a.s.ademiloye@swansea.ac.uk (A.S. Ademiloye)

yield function to describe the matrix behavior. Our computational results demonstrate that the accuracy and robustness of the proposed model for predicting the elastoplastic fracture response of FRC structures. Furthermore, we observed that in comparison to the elastic phase field fracture model, the occurrence of fracture is delayed when an elastoplastic phase model is employed due to the complex interactions between the plastic dissipation energy and the fracture energy.

Keywords: Elastoplastic Fracture, Fiber-Reinforced Composites, Transversely Isotropic, Phase Field Modeling, Crack

1. Introduction

Fiber-reinforced composite (FRC) materials are widely recognized for their superior stiffness and strength compared to conventional isotropic materials, which allows them to dissipate more energy during the deformation process [1]. These characteristics make FRC materials an ideal solution for enhancing structural durability. With ongoing advancements in contemporary engineering, particularly in the aerospace, automotive and defence industries, there is an increasing demand for structures that are not only lighter and stronger but also more durable. This demand has further stimulated the application and development of FRC materials. However, during the operational lifespan of most FRC structures, complexities arise due to fracture phenomena resulting from the failure of both the matrix and fibers, which can be attributed to material defects, design flaws, and other factors. Consequently, establishing damage models becomes notably challenging in the context of FRC.

There are generally two approaches to simulating fracture behavior using numerical methods: the discrete method and the diffusive method. In the discrete method, the crack is considered a geometric entity or discontinuity within the displacement field. Since the crack propagates between elements, the accuracy of this approach strongly depend on the mesh quality. In this regard, Trädegård [2] developed a robust algorithm that re-partitions the geometry near the crack region at each loading step, although it requires a significant amount of computational time. As an alternative to avoid mesh dependency, Belytschko and Black [3] introduced the Extended Finite Element Method

(XFEM). This approach represents discontinuities within the computational domain by enriching shape functions with discontinuous properties, ensuring that the discontinuous field remains entirely independent of the mesh boundaries.

However, the aforementioned method becomes extremely costly when dealing with complex geometric structures, particularly in handling crack propagation paths that include initiation, merging, and branching. To overcome this limitation, the phase field method was developed by Bourdin et al.[4]. The phase field method is particularly suited to tackle such issues and has garnered widespread attention in the academic community due to the simplicity of its numerical implementation. In the phase field model, smooth boundaries are used to approximate the internal discontinuous boundary of the crack, thereby avoiding the complexity of tracking the crack propagation path typically required in traditional models.

The mathematical formulation of the phase-field method was initially proposed by Francfort and Marigo [5] for quasi-static elastic brittle fracture. This approach involves minimizing the total energy with respect to both the phase-field variable and the displacement field, resulting in a system of partial differential equations (PDEs). Subsequently, Bourdin et al. [4] introduced a regularized phase field method to facilitate numerical implementation. Amor [6] and Miehe [7] proposed anisotropic formulations for phase-field models, in which the strain energy is divided into positive and negative components. By appropriately selecting a degradation function that acts on tensile elasticity, the expansion of cracks under compressive stress was prevented.

After years of development and refinement, the phase-field method has significantly improved. Borden [8] proposed a fourth-order phase-field model for the variational formulation of brittle fracture. Compared to second-order phase-field models, this model can capture more regularities and produce more accurate numerical solutions. Given that the failure of fiber-reinforced composites (FRC) may manifest in various modes driven by different forces, it is inappropriate to simulate their fracture behavior using a single-phase field model. Wang et al. [9] proposes a unified phase-field model within the framework of the original phase-field theory. By embedding a universal fracture criterion in the proposed formulation, it can predict tensionshear and compressionshear

fractures under complex stress states, and it introduces a compressive failure strength to account for fracture under compression. Bleyer et al. [10] proposed an orthotropic damage model for longitudinally/transversely degraded materials based on a multiphase field approach, where several distinct degradation mechanisms are described by different damage variables. Additionally, the dissipated fracture energies of each damage variable remain independent, and the coupling of all damage mechanisms is achieved through the degradation of elastic stiffness. The simulation results obtained using their proposed model show good agreement with theoretical and experimental findings in literature. Furthermore, their model reproduced the characteristics of crack propagation in anisotropic materials, which cannot be achieved by a standard model employing a single damage variable.

Despite the advances in multiphase field model of FRC materials, the precision of their constitutive model could be enhanced by simultaneously considering plasticity since FRC materials could experience permanent deformation after unloading. Consequently, some researchers have adopted the combination of phase-field models with plasticity to capture the elasto-plastic mechanical response of solids. For instance, Miehe et al. [11] employed phase field models to simulate the transition from ductile to brittle fracture-fracture models in thermo-elastic-plastic solids such as metals and glassy polymers. They defined the driving force based on potential functions associated with critical values of elastic and plastic energy densities, as well as non-elastic state variables. This approach was applied to simulate the transition from brittle to ductile behavior in the dynamic failure processes of metals and the quasi-static crack analysis in glassy polymers. The results obtained from these simulations showed excellent agreement with experimental observations. Duda [12] proposed a phase field formulation for fracture in small-strain elastoplastic solids, where the elastic and fracture energies were described using classical brittle fracture equations, while the plastic energy was represented by accumulated plastic strain. They examined the problem of Type I crack propagation under yielding conditions and emphasized the importance of accurately characterizing the length scale parameter l when coupling the phase field model with plasticity to ensure the activation of cracks. This correct characterization of the length scale parameter is crucial for cap-

turing the interaction effects between plasticity and damage mechanisms. Ambati et al. [13] presented an elasto-plastic phase field model, wherein a notable feature is the introduction of plastic accumulated strain variables into the degradation function of tensile strain elastic energy, thereby coupling the evolution of the phase field with plastic strain. Fang et al. [14] proposed a variational formulation for a fracture phase field model considering multi-surface plasticity. They analyzed the influence of plastic yield functions and hardening effects on material behavior. Additionally, they implemented phase field modeling of elasto-plastic solids using the commercial software Abaqus, solving the fracture problem of elasto-plastic solids with phase field through an alternating algorithm that decouples the phase field and displacement fields.

However, the elasto-plastic fracture phase field models in the above-mentioned studies are confined to isotropic materials such as metal[15] and soil[16], and have not been extended to FRC, while a great deal of research has been focused on elastic properties prediction of FRC[17], as exemplified by the work of Li et al.[18][19], which concentrates on predicting crack patterns in FRC. The main idea of this paper is to introduce a transversely isotropic elasto-plastic constitutive model [20][21], which describes the yielding of the matrix in FRC under the assumption that fiber plastic deformation is negligible, thereby capturing the nonlinear mechanical response of FRC under quasi-static loading conditions.

To address this gap, we propose a novel multiphase-field model to simulate elasto-plastic fracture in fiber-reinforced composites under quasi-static loading, focusing on the distinct failure mechanisms of fibers and matrix while neglecting interfacial effects. The models core feature lies in the thermodynamically consistent coupling between crack phase-field evolution and plastic strain accumulation. By employing different driving forces, the damage evolution equations for each phase field are decoupled, enabling independent characterization of fiber and matrix fracture. Numerical examples demonstrate that this approach accurately captures crack initiation within plastic strain localization zones and predicts key characteristics of quasi-static ductile fracture, including the crack nucleation site and trajectory in tensile specimens.

The remainder of the paper is organized as follows. In Section 2, we first provide

a detailed derivation of the multiphase field model for FRC. In Section 3, we discussed the discretization and numerical implementation of the governing differential equations. In Section 4, we validate the proposed model by comparing experimental and simulated numerical results, predicting the elasto-plastic fracture behavior of curved FRC. Furthermore, we investigated the crack evolution behavior of FRC plates with different topological types. Finally, conclusions are given in Section 5.

2. Phase Field Model

2.1. Multiple Phase Field Model of Elastic Solids Revisited

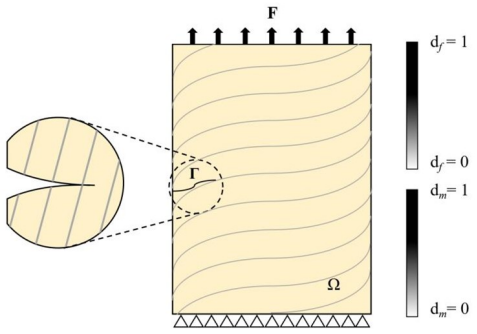

Fig. 1. The phase field representation for cracks.

Following Geelen and co-workers' variational description of a cracked solid [22] depicted in Figure 1, the total potential energy of an arbitrary elastic body Ω is formulated as the sum of the elastic strain energy and the fracture energy.

$$\Pi(\boldsymbol{u}, \Gamma) = \int_{\Omega} \varphi(\varepsilon(\boldsymbol{u}))\mathrm{d}\Omega + \int_{\Gamma} G_c \mathrm{d}\Gamma. \tag{1}$$

where Γ represents a set of internal discontinuous cracks, ε denotes the strain tensor, $\boldsymbol{u}$ represents the displacement vector at any location within the domain, φ denotes the elastic strain energy density, and G_c represents the critical fracture energy release rate.

Talreja and Ramesh [23] advanced a classical laminate theory under plane stress

conditions. The stress tensor of fiber-reinforced composite plate is defined as

$$\boldsymbol{\sigma} = \boldsymbol{C}_0 : \boldsymbol{\varepsilon}, \tag{2}$$

$$\boldsymbol{C}_0 = \begin{bmatrix} C_{11} & C_{12} & 0 \\ C_{12} & C_{22} & 0 \\ 0 & 0 & G_{12} \end{bmatrix}, \tag{3}$$

with

$$C_{11} = \frac{E_{11}}{1-\nu_{12}\nu_{21}}, C_{12} = \frac{\nu_{12}E_{22}}{1-\nu_{12}\nu_{21}}, C_{22} = \frac{E_{11}}{1-\nu_{12}\nu_{21}} \tag{4}$$

where $\boldsymbol{C}_0$ is the stiffness matrix of the elastic material, E_{11} represents the longitudinal elastic modulus, E_{22} represents the transverse elastic modulus, G_{12} represents the shear modulus, ν_{12} represents the in-plane Poisson's ratios.

In Griffith's brittle fracture theory, the energy needed to form a unit area of a fracture surface is equal to the critical fracture energy density G_c. The fracture energy in equation (1) corresponds to a sharp crack path, which is regularized by a diffusive crack phase field. We can approximate the crack surface using the phase field variable d. If the material is in a fully intact state, the phase field variable $d = 0$, while in the fully fractured state, $d = 1$.

Through the multiphase field model, the regularized fracture energy can be expressed as

$$\int_\Gamma G_c \mathrm{d}\Gamma = \int_\Omega G_c \gamma(d, \nabla d)\mathrm{d}\Omega, \tag{5}$$

where γ denotes the density functional of the crack surface. Using the second order structure tensors [24], the density functional of the crack surface is extended to isotropic materials

$$\begin{cases} \gamma_f(d_f, \nabla d_f) = \dfrac{1}{2l}d_f^2 + \dfrac{1}{2}l \cdot \nabla d_f \cdot \boldsymbol{D}_f \cdot (\nabla d_f)^T \\ \gamma_m(d_m, \nabla d_m) = \dfrac{1}{2l}d_m^2 + \dfrac{1}{2}l \cdot \nabla d_m \cdot \boldsymbol{D}_m \cdot (\nabla d_m)^T \end{cases}, \tag{6}$$

where l is a length scale parameter that determines the width of the smooth transition of the crack. The value of l must be at least twice the mesh length, as described in Ref.

[25]. The structure tensors $\boldsymbol{D}_f$ and $\boldsymbol{D}_m$ representing fiber failure and matrix failure, respectively, can be described as:

$$\begin{cases} \boldsymbol{D}_f = \alpha_1 \boldsymbol{n}_2 \otimes \boldsymbol{n}_2 \\ \boldsymbol{D}_m = \alpha_2 \boldsymbol{n}_1 \otimes \boldsymbol{n}_1 \end{cases}, \tag{7}$$

where $\boldsymbol{n}_1$ represents the principal direction of higher material fracture toughness and strength and the coefficients and are used to determine crack propagation.

To avoid physically inconsistent compressive cracking and to prevent interpenetration of crack surfaces under compression, the elastic energy density into two parts[7], which includes a "positive" part associated with tensile damage and a "negative" part associated with compression, which remains undegraded. For fiber,

$$\varphi_f(\varepsilon, d_f) = g(d_f)\varphi_f^+ + \varphi_f^-, \tag{8}$$

and for matix,

$$\varphi_m(\varepsilon, d_m) = g(d_m)\varphi_m^+ + \varphi_m^-. \tag{9}$$

where $g_i(d)$ represents the degradation function, which can be used to simulate the reduction in material stiffness due to crack propagation, and is described as:

$$g(d_i) = (1 - d_i)^2 + k, \quad i = f, m. \tag{10}$$

The terms φ_f^+,φ_m^+ are given by

$$\begin{cases} \varphi_f^+ = \dfrac{1}{2}\left(\overline{\boldsymbol{\varepsilon}}^+\right)^T \boldsymbol{C}_f \left(\overline{\boldsymbol{\varepsilon}}^+\right) \\ \varphi_m^+ = \dfrac{1}{2}\left(\overline{\boldsymbol{\varepsilon}}^+\right)^T \boldsymbol{C}_m \left(\overline{\boldsymbol{\varepsilon}}^+\right) + \left(\overline{\boldsymbol{\varepsilon}}^+\right)^T \boldsymbol{C}_m \left(\overline{\boldsymbol{\varepsilon}}^-\right) \end{cases}. \tag{11}$$

with

$$\boldsymbol{C}_f = \begin{bmatrix} C_{11} & 0 & 0 \\ 0 & 0 & 0 \\ 0 & 0 & 0 \end{bmatrix}, \boldsymbol{C}_m = \begin{bmatrix} 0 & C_{12} & 0 \\ C_{12} & C_{22} & 0 \\ 0 & 0 & G_{12} \end{bmatrix} \tag{12}$$

In this approach, only the strain energy generated by tensile stress is allowed to degrade,

$$\Pi(\boldsymbol{u}, d) = \sum_{i=f,m} \left\{ \int_{\Omega} \left[g(d_i)\varphi^{+}(\boldsymbol{\varepsilon}^{+}(\boldsymbol{u})) + \varphi^{-}(\boldsymbol{\varepsilon}^{-}(\boldsymbol{u})) \right] \mathrm{d}\Omega \right\} + \sum_{i=f,m} \left\{ \int_{\Gamma} G_c \gamma(d_i, \nabla d_i) \mathrm{d}\Gamma \right\}, \tag{13}$$

According to the principle of maximum thermodynamic dissipation [26], the evolution equations of the crack phase field is derived as follows

$$\begin{cases} 2(1-d_f)\varphi_f^{+} - G_{c,f}[\dfrac{d_f}{l_f} - l_f \cdot \nabla d_f \cdot \boldsymbol{D}_f \cdot (\nabla d_f)^T] = 0 \\ 2(1-d_m)\varphi_m^{+} - G_{c,m}[\dfrac{d_m}{l_m} - l_m \cdot \nabla d_m \cdot \boldsymbol{D}_m \cdot (\nabla d_m)^T] = 0 \end{cases}. \tag{14}$$

To simplify the treatment of the phase field equation and ensure the irreversibility of crack phase field during loading, we introduce the following local historical variables, P_f and P_m, by defining a history field function,

$$\begin{cases} P_f = \max \varphi_f^{+}(\boldsymbol{\varepsilon}(\boldsymbol{u})) \\ P_m = \max \varphi_m^{+}(\boldsymbol{\varepsilon}(\boldsymbol{u})) \end{cases}. \tag{15}$$

2.2. Phase Field Model of Fracture Coupled with Plasticity

When a solid material undergoes fracture, it is accompanied by significant plastic deformation. The total strain $\boldsymbol{\varepsilon}_{total}$ can be decomposed into the elastic strain component $\boldsymbol{\varepsilon}_e$ and the plastic strain component $\boldsymbol{\varepsilon}_p$,

$$\boldsymbol{\varepsilon}_{total} = \boldsymbol{\varepsilon}_e + \boldsymbol{\varepsilon}_p. \tag{16}$$

To compute the elastic-plastic fracture response, it is necessary to establish a connection between the evolution of damage and plastic deformation. To achieve this, the elastic energy density function φ_e and the plastic energy density function φ_p are defined to

express the total free energy density of the damaged elastic-plastic material φ_{total},

$$\varphi_{total} = \varphi_e(\boldsymbol{\varepsilon}_e, p) + \varphi_p(\overline{\boldsymbol{\gamma}}, d) \tag{17}$$

$$\varphi_p(\overline{\boldsymbol{\gamma}}, d) = \frac{1}{2} H(d) \overline{\boldsymbol{\gamma}}^2, \tag{18}$$

where $\overline{\boldsymbol{\gamma}}$ represents the equivalent plastic strain, and H denotes the hardening modulus. The dissipative energy of the material includes both plastic dissipation energy and fracture dissipation energy. The plastic dissipation energy density can be expressed as

$$\phi_p(\overline{\boldsymbol{\gamma}}, d) = \sigma_y(d) \overline{\boldsymbol{\gamma}}, \tag{19}$$

Therefore, the total internal energy density

$$\Pi(\boldsymbol{u}, d) = \varphi_e(\boldsymbol{\varepsilon}_e, d) + \varphi_p(\overline{\boldsymbol{\gamma}}, d) + \phi_p(\overline{\boldsymbol{\gamma}}, d) + \int_\Omega G_c \gamma(d, \nabla d) \mathrm{d}\Omega, \tag{20}$$

The elasto-plastic damage is governed by the same degradation function $g(d)$. To simplify the treatment of phase field equations and ensure the irreversibility of the crack phase field during loading, the following history field function

$$P_m = \max \varphi_m^+(\boldsymbol{\varepsilon}(\boldsymbol{u})) + \frac{1}{2} H \overline{\boldsymbol{\gamma}}^2 + \sigma_y \overline{\boldsymbol{\gamma}}. \tag{21}$$

where σ_y represents the yield stress. We assume that the material follows an ideal plasticity model and exhibits linear isotropic hardening characteristics. The yield function is defined as follows

$$F = f - \sigma_y < 0. \tag{22}$$

We assume that the material properties of the fiber reinforced composites are transversely isotropic[20]. Additionally, the following matrix yield criterion is adopted

$$f = \sqrt{\frac{1}{6}(\sigma_{22} - \sigma_{33})^2 + \sigma_{12}^2 + N\sigma_{23}^2 + \frac{\mu}{2}(\sigma_{22} + \sigma_{33})}, \tag{23}$$

μ and N are employed to replace the tensile and compressive yield strengths, as they provide a more accurate representation of tensile yielding. The numerical value of μ depends on the yield stresses used in the calculation, while N is assumed to be 1 in this study[27].

3. Implementation

3.1. Finite Element Implementation

This section presents the finite element discretization procedure for the elasto-plastic phase field model. During the finite element discretization, the displacement u, damage parameters d_f and d_m are typically represented using interpolation functions and the nodal values of displacement and phase field. Each element is defined by four corresponding nodal elements, as shown in equation (24).

$$\begin{cases} u = \boldsymbol{N}^u \boldsymbol{u}^e = \sum_{i=1}^{n} \boldsymbol{N}_i^u \boldsymbol{u}_i^e \\ \boldsymbol{d}_f = \boldsymbol{N}^d \boldsymbol{d}_f^e = \sum_{i=1}^{n} \boldsymbol{N}_{f,i}^d \boldsymbol{d}_{f,i}^e \\ \boldsymbol{d}_m = \boldsymbol{N}^d \boldsymbol{d}_m^e = \sum_{i=1}^{n} \boldsymbol{N}_{m,i}^d \boldsymbol{d}_{m,i}^e \end{cases}, \tag{24}$$

where $\boldsymbol{N}^u$ and $\boldsymbol{N}^d$ are the interpolation matrices of shape functions. The displacement and phase field damage parameters in this study adopt the same shape functions. The parameters u^e, d_f^e, and d_m^e represent the nodal values of displacement and phase field within the element, where n denotes the number of nodes within the element. $\boldsymbol{B}^u$ and $\boldsymbol{B}^i$ $(i = f, m)$ are differential matrices for displacement and phase field, as given in the form of equation (25).

$$\begin{cases} \boldsymbol{\varepsilon} = \boldsymbol{B}^u \boldsymbol{u}^e \\ \nabla d_f = \boldsymbol{B}^f \boldsymbol{d}_f^e \\ \nabla d_m = \boldsymbol{B}^m \boldsymbol{d}_m^e \end{cases}. \tag{25}$$

The residual vector $\boldsymbol{R}$, corresponding to the stress equilibrium at the element level and the evolution of the phase field, can be expressed using the following combination equation, as shown in the form of (26). Additionally, to prevent crack healing that violates physical laws, the maximum history functions P_i $(i = f, m)$ are introduced in this context.

$$\begin{cases} \boldsymbol{R} = \int_\Omega \boldsymbol{B}^u \sigma \mathrm{d}\Omega - \int_\Omega \boldsymbol{N}^u f \mathrm{d}\Omega \\ \boldsymbol{R}_f = -\int_\Omega \{[2(1-d_f)P_f - \frac{d_f}{l_f}]\boldsymbol{N}^d - l_f \cdot \boldsymbol{B}^{d_f} \cdot D_f \cdot \nabla d_f\}\mathrm{d}\Omega \\ \boldsymbol{R}_m = -\int_\Omega \{[2(1-d_m)P_m - \frac{d_m}{l_m}]\boldsymbol{N}^d - l_m \cdot \boldsymbol{B}^{d_m} \cdot D_m \cdot \nabla d_m\}\mathrm{d}\Omega \end{cases} . \tag{26}$$

It is evident that the governing system is a coupled problem. To address this issue, researchers have proposed and employed two methods: staggered iteration and monolithic computation. In this study, we use the staggered iteration algorithm to improve convergence speed. In this approach, multiple iterations are performed for each small load increment, resulting in higher efficiency compared to purely staggered methods. The main process of the iterative staggered algorithm is shown in Algorithm 1. Due to the adoption of the staggered method, the linear system of the displacement increment step equations are formulated as follows.

By introducing the finite element discretization above, where $\boldsymbol{K}$ represents the stiffness matrix, $\boldsymbol{K}_f$ and $\boldsymbol{K}_m$ denote the phase field matrices, and $\boldsymbol{E}^{epc}$ is the elasto-plastic Jacobian matrix, as given in (27). Due to the nonlinear property of the system of equations, an incremental iterative scheme is employed for computation.

$$\begin{cases} \boldsymbol{K} = \dfrac{\partial \boldsymbol{R}}{\partial \boldsymbol{u}^e} = \int_\Omega [(1-d)^2 + k](\boldsymbol{B}^u)^T \boldsymbol{E}^{epc} \boldsymbol{B}^u \mathrm{d}\Omega \\ \boldsymbol{K}_f = \dfrac{\partial \boldsymbol{R}_f}{\partial \boldsymbol{d}_f^e} = \int_\Omega \{G_c l (\boldsymbol{B}^f)^T + [\frac{G_c}{l} + 2P_f](\boldsymbol{N}^f)^T \boldsymbol{N}^f\}\mathrm{d}\Omega \\ \boldsymbol{K}_m = \dfrac{\partial \boldsymbol{R}_m}{\partial \boldsymbol{d}_m^e} = \int_\Omega \{G_c l (\boldsymbol{B}^m)^T + [\frac{G_c}{l} + 2P_m](\boldsymbol{N}^m)^T \boldsymbol{N}^m\}\mathrm{d}\Omega \end{cases} . \tag{27}$$

To decouple the phase field and displacement field, the programming procedure shown

in Algorithm 1 is employed. For the plane stress model studied in this paper, the displacement $\boldsymbol{u}$ has two degrees of freedom in two directions, while the damage variables $\boldsymbol{d}_f$ and $\boldsymbol{d}_m$ for the phase field have one degree of freedom.

Firstly, we initialize the phase field scalar variables $\boldsymbol{d}_{f,0}$ and $\boldsymbol{d}_{m,0}$, as well as the maximum history functions P_i $(i = f, m)$ at each node element. We set the initial nodal displacement values $\boldsymbol{u}_0 = 0$, and adopt the staggered iteration algorithm in each iteration. Specifically, in each iteration, the history field function P is updated based on the current displacement field and phase field values. The displacement increment is added to the current displacement value to update the displacement field $\boldsymbol{u}_{n-1}$. Using the updated displacement field, the phase field variables $\boldsymbol{d}_{f,n}$ and $\boldsymbol{d}_{m,n}$ are computed. Then, utilizing the updated phase field values, the displacement increment system of equations is solved using the staggered iteration method. Finally the displacement field $\boldsymbol{u}_n$ is calculated and updated and the convergence criteria are checked. Through these steps, the algebraic equations (28) are solved.

$$\begin{cases} \boldsymbol{K}(\boldsymbol{u}_n, \boldsymbol{d}_{f,n}, \boldsymbol{d}_{m,n})\boldsymbol{u}_{n+1} = \boldsymbol{F}_{u,n+1} \\ \boldsymbol{K}_f(\boldsymbol{u}_{n+1}, \boldsymbol{d}_{f,n})\boldsymbol{d}_{f,n+1} = \boldsymbol{F}_{f,n+1} \\ \boldsymbol{K}_m(\boldsymbol{u}_{n+1}, \boldsymbol{d}_{m,n})\boldsymbol{d}_{m,n+1} = \boldsymbol{F}_{m,n+1} \end{cases} . \tag{28}$$

3.2. Plastic Return Mapping Implementation

The core of the material model's numerical implementation is the stress update procedure, known as the return mapping algorithm. It operates on the principle of an elastic predictor and a plastic corrector. The algorithm proceeds as follows:

The process begins with an elastic predictor step, where a trial stress state is computed assuming purely elastic behavior:

$$\boldsymbol{\sigma}_{trial} = \boldsymbol{C}^e : \left(\boldsymbol{\varepsilon} - \boldsymbol{\varepsilon}_p^{old}\right). \tag{29}$$

A yield condition check is then performed:

$$f_{trial} = F(\boldsymbol{\sigma}_{trial}, \overline{\varepsilon}_p^{old}). \tag{30}$$

Algorithm 1 Solution Procedure for the Elasto-plastic Phase Field Model

Intitialize $\boldsymbol{u}, \boldsymbol{d}_f, \boldsymbol{d}_m, \gamma, u_{eps} = 10^{-4}, d_{eps} = 10^{-3}, k_{max}, f, \sigma_y$;
for $n = 1$ to nototal (loop loading steps) **do**
  $k = 0$;
  while $f > \sigma_y$ **do**
    Compute γ;
  end while
  while $u^e > u_{eps}$ or $d^{e,f} > d_{eps,f}$ or $d^{e,m} > d_{eps,m}$ or $k < k_{max}$ **do**
    Update integration counter: $k = k + 1$;
    Computer $\boldsymbol{u}^k$, $\boldsymbol{d}^{k,f}$, $\boldsymbol{d}^{k,m}$, P by solving (28);
    Evaluate the residuals $u^e = \|\boldsymbol{u}^k - \boldsymbol{u}^{k-1}\|/\|\boldsymbol{u}^{k-1}\|$, $d^{e,f} = \|\boldsymbol{d}^{k,f} - \boldsymbol{d}^{k-1,f}\|/\|\boldsymbol{d}^{k-1,f}\|$, $d^{e,m} = \|\boldsymbol{d}^{k,m} - \boldsymbol{d}^{k-1,m}\|/\|\boldsymbol{d}^{k-1,m}\|$;
  end while
  Set $\boldsymbol{u}_n = \boldsymbol{u}^k$, $\boldsymbol{d}_{n,f} = \boldsymbol{d}^{k,f}$, $\boldsymbol{d}_{n,m} = \boldsymbol{d}^{k,m}$;
end for

If $f_{trial} < 0$,the step is elastic, and the trial state is accepted:$\boldsymbol{\sigma}_{new} = \boldsymbol{\sigma}_{trial}$.If$f_{trial} > 0$, plastic deformation occurs, necessitating a plastic correction. For associative plasticity, the plastic flow rule is:

$$\Delta\boldsymbol{\varepsilon}_p = \Delta\gamma \frac{\partial F}{\partial \boldsymbol{\sigma}}. \tag{31}$$

The updated stress and equivalent plastic strain are then:

$$\boldsymbol{\sigma}_{new} = \sigma_{trial} - \boldsymbol{C}^e : \Delta\boldsymbol{\varepsilon}_p, \bar{\varepsilon}_p^{new} = \bar{\varepsilon}_p^{old} + \Delta\gamma. \tag{32}$$

The plastic multiplier$\Delta\gamma$is found iteratively to satisfy the consistency condition$F(\boldsymbol{\sigma}_{new}, \bar{\varepsilon}_p^{new}) = 0$. The consistent tangent modulus, crucial for the global Newton-Raphson method, is derived from the linearization of this algorithm:

$$\boldsymbol{C}^{ep} = \frac{\partial \boldsymbol{\sigma}_{new}}{\partial \boldsymbol{\varepsilon}}. \tag{33}$$

4. Model validation with experimental results

4.1. Tensile Tests of Axisymmetrically Notched Specimen

Firstly, in order to verify the effectiveness of this method, we designed two cases to study the fracture behavior of isotropic materials using the elasto-plastic fracture phase field method. In the first case study which involves an asymmetrical notch specimen, we studied the influence of the coupling between the phase field and equivalent plastic strain under unidirectional tensile load on the numerical results. Furthermore, we investigated the the ability of our proposed model to detect and track crack initiation and subsequent crack growth.

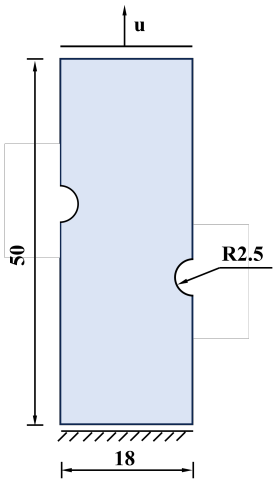

Fig. 2. Axisymmetrically notched specimen. All dimensions are given in mm.

The computational model, as shown in Figure 2, has dimensions of 1.0 mm×18 mm×50 mm with a hole radius of 2.5 mm. The center of the hole is located 20 mm away from the edge. The material properties of the specimen are as follows: Elastic modulus $E = 71.48$ GPa, Poisson's ratio $\nu = 0.3$, initial yield stress $\sigma_{y0} = 345$ MPa, critical fracture energy density $G_c = 9.31$ MPa/mm, hardening modulus $H = 714.8$ MPa [28]. The mesh is refined in areas where cracks may occur, and the phase field crack width parameter l is set to 0.2 mm. To facilitate convergence, the paper adopts a displacement increment of 3.0×10^{-5} mm.

As illustrated in Figure 3, the crack initially appears at two asymmetric notche in the elastic phase field model and begins to propagate in parallel. These notches are locations of elastic stress concentration. Then the crack gradually extends towards the center of the specimen, creating a crack path that does not conform to physical principles as well as real-world observations.

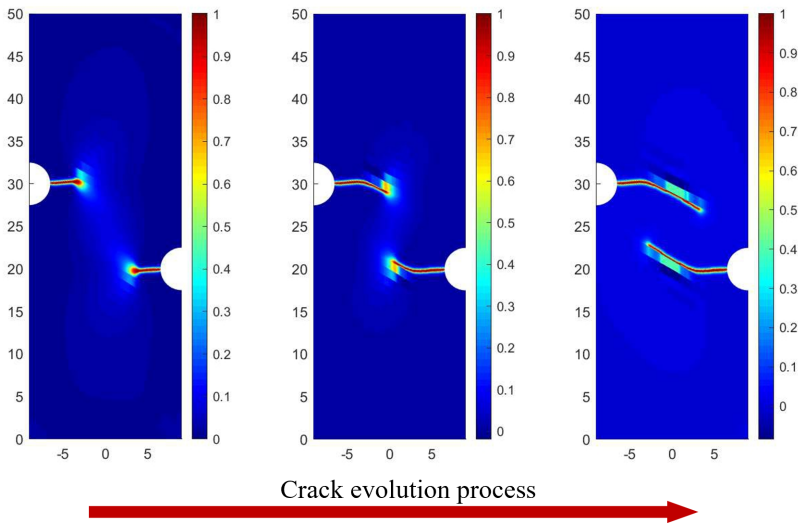

Fig. 3. Phase-field fracture simulation uncoupled from plastic strain

The results of the aforementioned model overlook the plastic deformation occurring at the crack tip. However, the evolution of the phase field's shape, position, and size is related to the plastic zone. Therefore, it is essential to incorporate the equivalent plastic strain and include the plastic crack driving force in the total energy equation. In contrast, according to our model, the evolution of the crack phase field is driven by the plastic strain localization occurring at the asymmetric notch of the specimen. Unlike uncoupled models, the proposed model accurately captures the fracture evolution process governed by realistic physical laws as shown in Figure 4, which are highly consistent with the numerical results of Ambati [13] and Fang et al. [29]. When the displacement increment is accumulated close to 0.19 mm, the specimen structure is fractured.

The excellent agreement between our simulation and the reference data validates

the effectiveness of the proposed elasto-plastic phase field model. More importantly, it demonstrates the core coupling mechanism: the evolution of the crack phase field is driven by plastic strain localization. The plastic dissipation energy competes with the fracture energy, which delays crack initiation and alters the propagation path significantly compared to the uncoupled elastic model. This underscores the necessity of incorporating plasticity to accurately capture the ductile fracture behavior in solids.

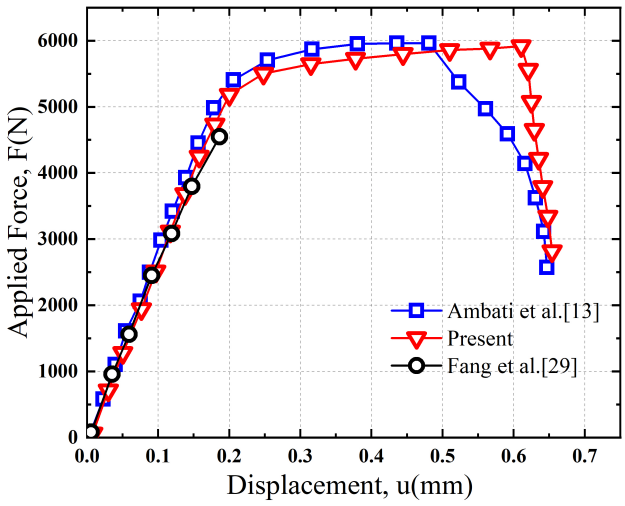

Fig. 4. Elasto-plastic deformation force-displacement curve under uniaxial tension.

Figure 5 illustrates the comparison between the crack propagation process obtained in this study and the one reported in reference [29]. The model successfully predicts the initiation of cracks at the notch, and it is evident that the initial crack nucleates at the stress concentration points of the two circular notches. Due to the influence of plastic hardening modulus, the crack path initially expands horizontally and then extends diagonally along the diagonal direction, ultimately resulting in the complete failure of the specimen structure. The above data and comparison of crack propagation demonstrate the effectiveness of the model and algorithm described in this paper.

Subsequently, we will validate the elastoplastic fracture phase field model presented

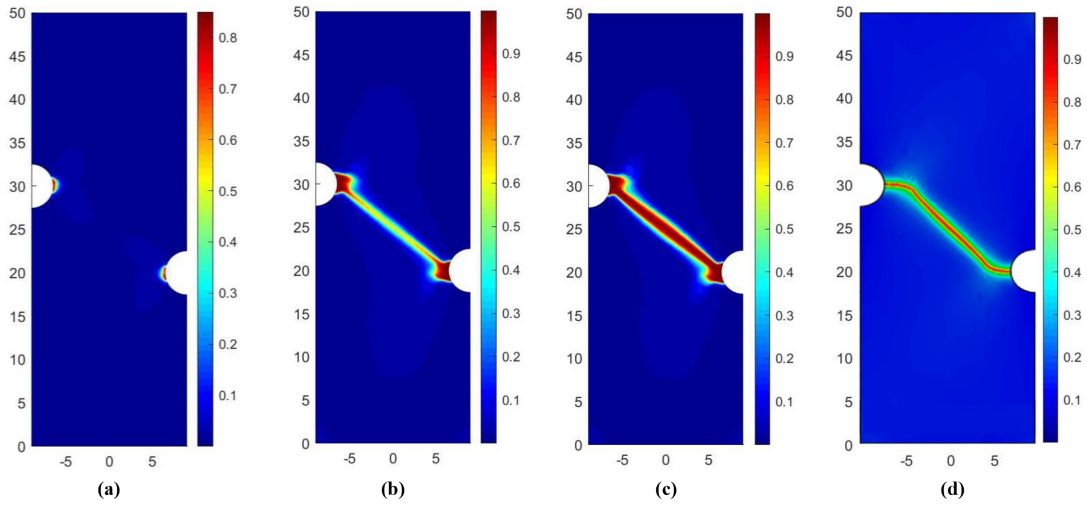

Fig. 5. Schematic illustration of the phase-field crack propagation process in a specimen using the proposed model. (a) load step 50, (b) load step 73, (c) load step 80, (d) Comparison with Fang's results[29].

in this paper by comparing it with the experimental and simulation data results by Pillai et al. [30]. In the computational model shown in Figure 6, a prescribed open crack is placed horizontally in the plate. The size of the model are 1.0 mm×65 mm×60 mm. The material properties of the plate are as follows: Elastic modulus $E = 61400$ MPa, Poisson's ratio $\nu = 0.042$, critical fracture energy density $G_c = 65.4$ MPa/mm, shear modulus $\mu_{12} = 3782$ MPa.

The final damage contour of the simulation sample and the predicted stress-strain response are compared with the experimental results shown in Figures 7 and 8. From the force-displacement response, it can be observed that after entering plastic deformation, the model yields with the accumulation of strain increments and exhibits significant plastic deformation prior to fracture. From Figure 8, it can be observed that once the strain load reaches its peak, the simulated response shows destabilization and unstable crack propagation.

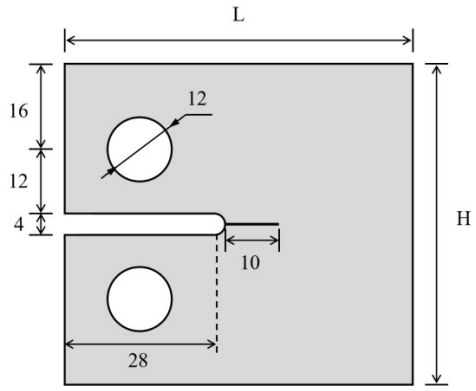

Fig. 6. Schematic illustration of the plate with precribed open crack.

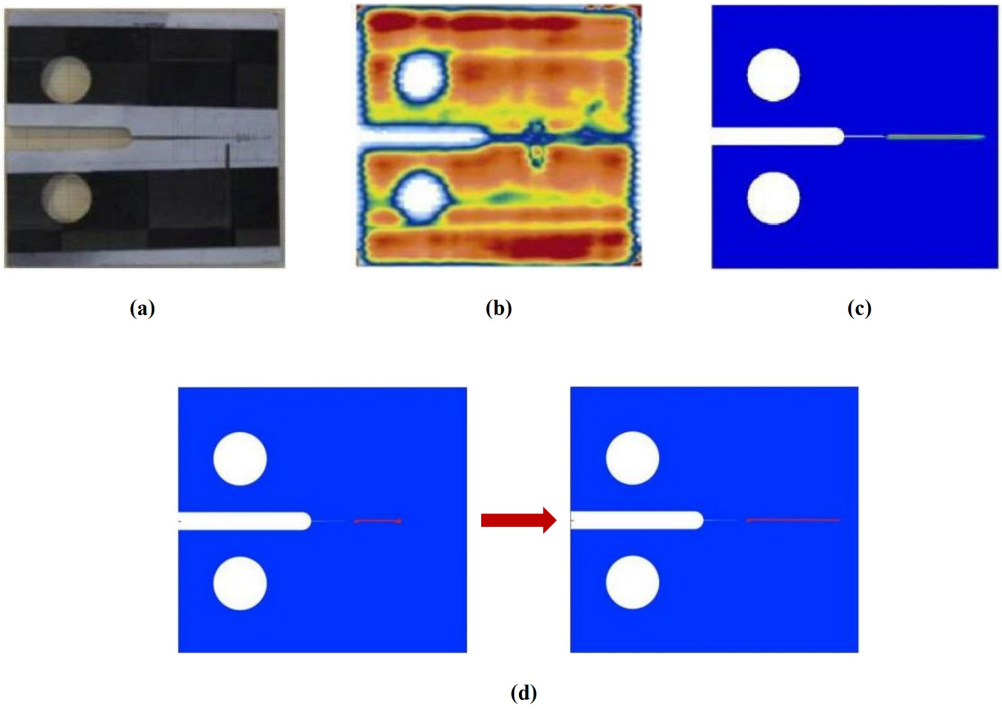

Fig. 7. (a) Photograph of the crack path in the specimen. (b) CT scan image of the crack in the specimen. (c) Comparison of crack paths obtained from the cohesive phase-field model. (d) Crack evolution process based on the proposed model.

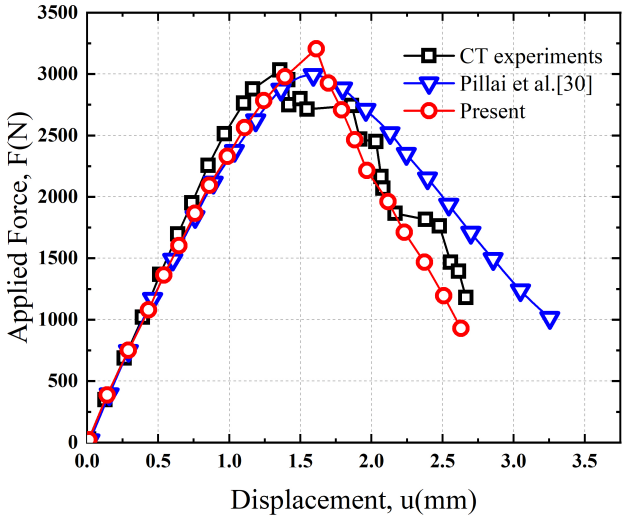

Fig. 8. The experimental data compared to the fracture phase-field model algorithm.

4.2. Tensile Tests of Unidirectional Fiber Reinforced Composite Material Laminae

In this section, we investigate the tensile behavior of unidirectional FRC plates. By performing fracture analysis on FRC plate with a central circular hole, we further demonstrate the capability of the elastic-plastic phase field model in simulating fracture of FRC.

The specimen for this section is illustrated in Figure 9, in size of 1.0 mm× 18 mm× 80 mm. The radius of the hole is 2.5 millimeters, and its distance from the edge is 20 mm. The material parameters are as follows: the longitudinal elastic modulus E_{11} is 26.5 GPa, the transverse elastic modulus E_{22} is 2.6 GPa, the shear modulus G_{12} is 1.3 GPa, the Poisson's ratio v is 0.35, the longitudinal fracture energy $G_{c,f}$ is 31.1 N/mm, the transverse fracture energy $G_{c,m}$ is 0.622 N/mm, and the shear fracture energy $G_{c,II}$ is 0.472 N/mm. The transverse tensile strength of this material is $\sigma_{22} = 20.25$ and the phase field crack width parameter l is set to 0.4 mm. The displacement loading increment is set to 3.0×10^{-5} mm. These material properties were taken from Ref.[30]

As shown in Figure 10, the predicted strengths by the proposed method show good agreement with the results from [30], Zhang [31], and Moodniks [32]. This consistency

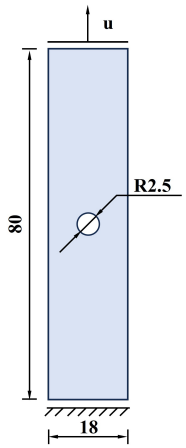

Fig. 9. FRC plate with a central circular hole. All dimensions are given in mm.

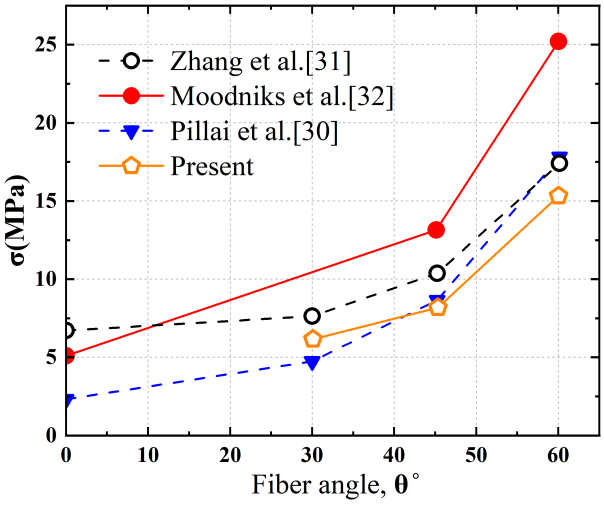

Fig. 10. Comparison of fracture strength at different fiber angles.

lends support to the reliability of the present approach.

Furthermore, this study predicts the initiation and propagation paths of cracks in FRC plates with circular holes. The fracture simulations of straight fibers with fiber angles of 30° are shown in Figure 11, while those with fiber angles of 45° are shown in Figure 12, and the simulations for fiber angles of 60° are presented in Figure 13. We observe that for materials with three different fiber angles, the initial crack nucleates at stress concentration points and subsequently propagates diagonally along the respective fiber angles, ultimately resulting in the complete failure of the specimen structure during the tensile test.

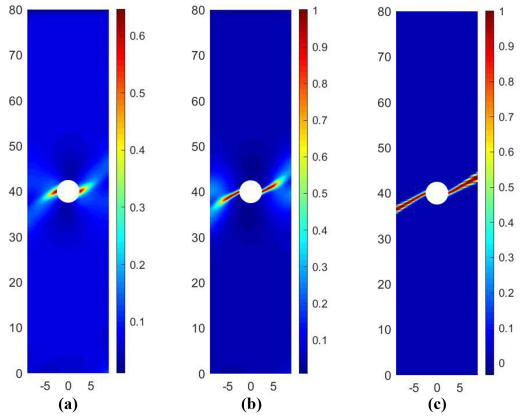

Fig. 11. Phase-field simulation of crack evolution in a 30° straight fiber-reinforced composite plate: (a) load step 90, (b) load step 99, (c) load step 100.

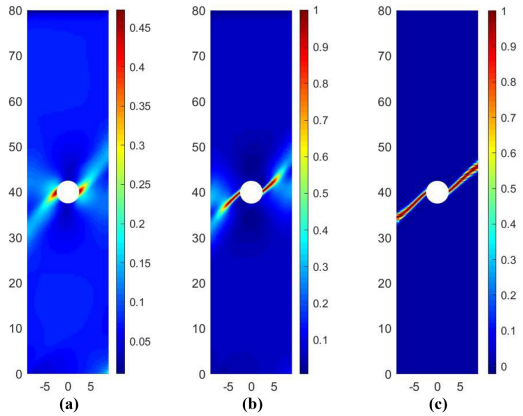

Fig. 12. Phase-field simulation of crack evolution in a 45° straight fiber-reinforced composite plate: (a) load step 100, (b) load step 115, (c) load step 120.

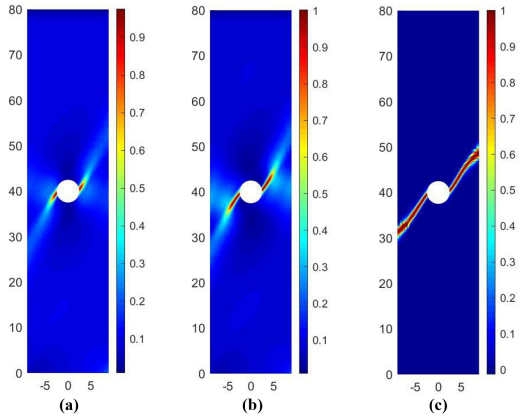

Fig. 13. Phase-field simulation of crack evolution in a 30° straight fiber-reinforced composite plate: (a) load step 80, (b) load step 86, (c) load step 120.

These results collectively demonstrate the dominant influence of fiber architecture on the fracture behavior of unidirectional composites. The simulations confirm that the fiber orientation is the primary factor controlling both the crack path and the structural strength. Cracks initiate at stress concentration points and propagate strictly along the fiber direction. A larger fiber angle, which aligns the fibers closer to the tensile

loading direction, results in a higher effective stiffness and, consequently, a greater peak load capacity. This is because the fibers bear the tensile load more efficiently when their alignment is more parallel to the applied force. The observation that cracks lose initiation symmetry at irregular pores and preferentially nucleate at locations with the highest local curvature further validates the model's capability to capture the complex physical interactions between the transverse isotropy and geometric defects of FRC.

4.3. Modeling the Failure Behaviors of Curved Fiber Reinforced Composite Material

In this section, we systematically investigates the unilateral tensile fracture of curved FRC plates and explores the influence of fiber path design variables on crack propagation paths and strength.

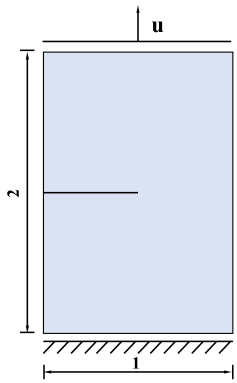

Fig. 14. Unilateral tensile plate with a pre-existing crack.

The model for this section is illustrated in Figure 14, with size of 1.0 mm×1 mm×2 mm. A pre-existing crack with a length of 0.5 mm is introduced in the plate. The model parameters are as follows[33]: the longitudinal elastic modulus E_{11} is 114.8 GPa, the transverse elastic modulus E_{22} is 11.7 GPa, the shear modulus G_{12} is 9.6 GPa, the Poisson's ratio ν is 0.21, the longitudinal fracture energy $G_{c,f}$ is 106.3 N/mm, the transverse fracture energy $G_{c,m}$ is 0.2774 N/mm, and the shear fracture energy $G_{c,II}$ is 0.7879 N/mm. The phase field crack width parameter l is set to 0.02 mm. The displacement loading increment is set at 3.0×10^{-5} mm.

We employs mathematical formulas to generate curved fiber paths to ensure the continuity. The schematic illustration of fiber paths is shown in Figure 15 [34], where the fiber orientation θ can be expressed as

$$\theta(x,y) = \begin{cases} \alpha + \dfrac{2(T_1 - T_0)}{L_0}|x' - iL_0| + T_0, & -\dfrac{L_0}{2} + iL_0 x' \leq \dfrac{L_0}{2} + iL_0 \\ \alpha + \dfrac{2(T_1 - T_0)}{L_0}|x' + iL_0| + T_0, & -\dfrac{L_0}{2} - iL_0 x' \leq \dfrac{L_0}{2} - iL_0 \end{cases}, \quad i = 0, 1, 2, ... \tag{34}$$

where x and y are global coordinates, x' and y' are reference coordinates, α is the angle between the two coordinate systems, T_0 and T_1 represent the trajectory directions at the fiber center and edge, respectively, and L_0 is the reference length.

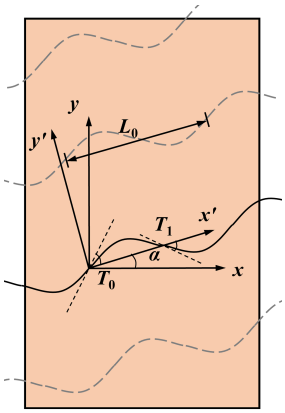

Fig. 15. Illustration of fiber paths.

No fiber fracture was observed after the matrix underwent plastic deformation failure. Therefore, unless otherwise specified in this study, the term *failure* refers to matrix failure.

To study the influence of the curved fiber angle on plastic deformation, we used the framework proposed in this paper to calculate the crack propagation and force-displacement relationship of the plate at three different angles. As shown in Figure 16, fiber-reinforced composite materials yield under higher strain conditions as the fiber angle increases and exhibit significant plastic deformation before fracture. This suggests

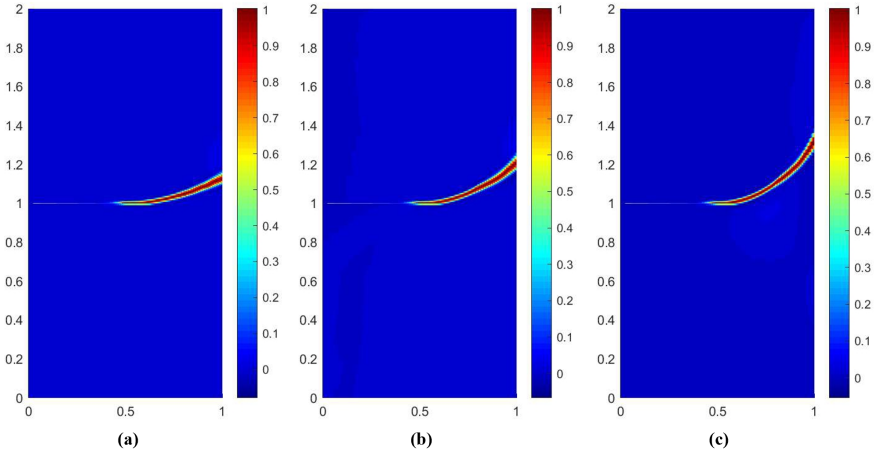

Fig. 16. (a): Crack propagation mode in $[30, 0]$ curved FRC plate; (b): Crack propagation mode in $[45, 0]$ curved FRC plate; (c): Crack propagation mode in $[60, 0]$ curved FRC plate.

that fibers play a pivotal role in controlling the material's fracture behavior. Furthermore, the crack propagation mode is no longer linear but instead consistently extends along the direction of the curved fiber.

This curved crack path, dictated by the spatially varying fiber orientation, is a key finding. It indicates that damage does not accumulate along a single dominant direction. Compared to straight-fiber composites, this leads to a more progressive failure process and enhanced post-peak structural stability, as evidenced by the more gradual load decrease in the force-displacement response.

This highlights the potential of fiber path design as an effective means of tailoring stable and damage-tolerant failure modes. Due to the continuously changing crack propagation path within the plate, the damage does not propagate in a specific direction along the FRC plate. Therefore, its strength is more designable compared to that of composites with straight fibers.

In this study, FRCs are simplified as homogenized transversely isotropic materials. Based on this simplification, the study considers the influence of plastic deformation on the displacement of the matrix phase and its progressive failure. Compared to the elastic phase field model for curved fiber composites, this approach more accurately reflects the

real physical processes of fracture.

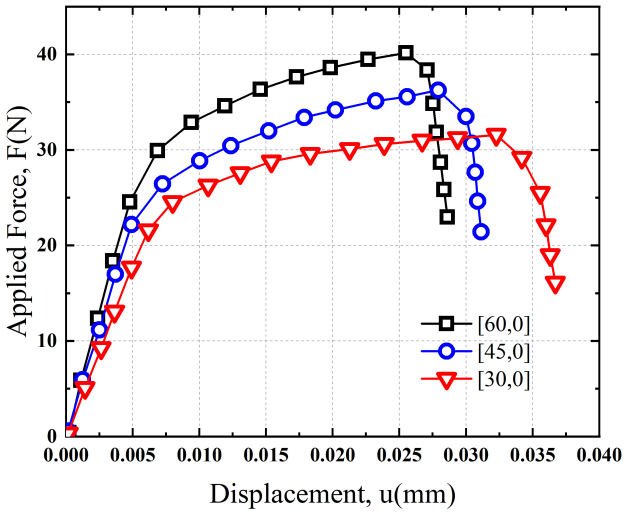

Fig. 17. Force-displacement diagram of curved FRC plate.

The load-displacement curve of the curved fiber-reinforced composite plate is shown in Figure 17. It shows that the increase of the initial angle of the fibers leads to an increase in the maximum tensile load, but also leads an earlier crack initiation. It also shows that as the angle of the curved fibers increases, the fibers bear a greater proportion of the load. And with the displacement load increasing, the matrix enters the plastic stage later. In fiber-reinforced composite materials, fibers are primarily responsible for bearing tensile loads, while the matrix mainly transmits shear and compressive forces. When external loads apply on the material, the fibers initially experience stress, which then subsequently transfer throughout the material via the matrix. With a larger fiber angle approaching 90 degrees, the fibers align nearly parallel to the direction of the load, enabling them to effectively withstand tensile forces. As a result, the stress on the matrix is relatively minor, requiring greater loads for the matrix to undergo plastic deformation.

It is evident that, compared to elastic phase field simulations, the phase field model incorporating matrix plasticity demonstrates superior load-bearing capacity in curved

fiber-reinforced composite plates. This is attributed to the accumulation of plastic strain at the crack tip location with increasing displacement. Additionally, the plastic dissipation energy resulting from plastic damage delays the accumulation of fracture energy required for fracture initiation. The interplay between these two factors significantly impacts the initiation and propagation of cracks in the FRC material.

This enhanced performance is attributed to the interplay between plastic and fracture dissipation. The accumulation of plastic strain at the crack tip consumes a portion of the external work that would otherwise contribute directly to crack propagation. This competition mechanism delays the accumulation of fracture energy required for crack initiation, thereby increasing the overall load-bearing capacity and stabilizing the failure process.

5. Conclusions

In this work, we have developed a phase field fracture model for transversely isotropic fiber-reinforced composites (FRC) with elasto-plastic matrix. The main findings can be summarized as follows:

A coupled phase field fracture model incorporating transversely isotropic plasticity has been successfully established, enabling independent description of fiber and matrix damage evolution. Model validation demonstrates that considering matrix plasticity leads to more physically realistic crack initiation locations and propagation paths, showing significant differences from pure elastic predictions.

Fiber orientation and path significantly influence the fracture behavior of FRC plates: straight fibers with larger angles exhibit higher load-carrying capacity, while curved fibers guide cracks along curved paths, enhancing damage tolerance.

Matrix plastic dissipation competes with fracture energy, delaying crack propagation and resulting in superior load-carrying capacity of curved fiber plates under elasto-plastic conditions compared to elastic predictions.

The proposed model provides a robust numerical tool for predicting complex fracture processes in FRC structures, offering valuable insights for material design and structural optimization.

Acknowledgments

This work was supported by NSFC under Grant No. 12272182. A.S. Ademiloye and Yang Zhang acknowledge the support provided by the Royal Society through the International Exchange Grant (IES\NSFC\223217).

References

[1] E. Martín-Santos, P. Maimí, E. V. González, P. Cruz, A continuum constitutive model for the simulation of fabric-reinforced composites, Composite Structures 111 (2014) 122–129.

[2] A. Trädegård, F. Nilsson, S. Östlund, Fem-remeshing technique applied to crack growth problems, Computer Methods in Applied Mechanics and Engineering 160 (1998) 115–131.

[3] T. Belytschko, T. Black, Elastic crack growth in finite elements with minimal remeshing, International journal for numerical methods in engineering 45 (1999) 601–620.

[4] B. Bourdin, G. A. Francfort, J.-J. Marigo, Numerical experiments in revisited brittle fracture, Journal of the Mechanics and Physics of Solids 48 (2000) 797–826.

[5] G. A. Francfort, J.-J. Marigo, Revisiting brittle fracture as an energy minimization problem, Journal of the Mechanics and Physics of Solids 46 (1998) 1319–1342.

[6] H. Amor, J.-J. Marigo, C. Maurini, Regularized formulation of the variational brittle fracture with unilateral contact: Numerical experiments, Journal of the Mechanics and Physics of Solids 57 (2009) 1209–1229.

[7] C. Miehe, M. Hofacker, F. Welschinger, A phase field model for rate-independent crack propagation: Robust algorithmic implementation based on operator splits, Computer Methods in Applied Mechanics and Engineering 199 (2010) 2765–2778.

[8] M. J. Borden, T. J. Hughes, C. M. Landis, C. V. Verhoosel, A higher-order phase-field model for brittle fracture: Formulation and analysis within the isogeometric

analysis framework, Computer Methods in Applied Mechanics and Engineering 273 (2014) 100–118.

[9] Q. Wang, Q. Yue, W. Zhou, Y. Feng, X. Chang, Modeling of both tensional-shear and compressive-shear fractures by a unified phase-field model, Applied Mathematical Modelling 117 (2023) 162–196.

[10] J. Bleyer, R. Alessi, Phase-field modeling of anisotropic brittle fracture including several damage mechanisms, Computer Methods in Applied Mechanics and Engineering 336 (2018) 213–236.

[11] C. Miehe, M. Hofacker, L.-M. Schänzel, F. Aldakheel, Phase field modeling of fracture in multi-physics problems. part ii. coupled brittle-to-ductile failure criteria and crack propagation in thermo-elasticplastic solids, Computer Methods in Applied Mechanics and Engineering 294 (2015) 486–522.

[12] F. P. Duda, A. Ciarbonetti, P. J. Sánchez, A. E. Huespe, A phase-field/gradient damage model for brittle fracture in elasticplastic solids, International Journal of Plasticity 65 (2015) 269–296.

[13] M. Ambati, T. Gerasimov, L. De Lorenzis, Phase-field modeling of ductile fracture, Computational Mechanics 55 (2015) 1017–1040.

[14] J. Fang, C. Wu, J. Li, Q. Liu, C. Wu, G. Sun, Q. Li, Phase field fracture in elasto-plastic solids: Variational formulation for multi-surface plasticity and effects of plastic yield surfaces and hardening, International Journal of Mechanical Sciences 156 (2019) 382–396.

[15] Y. Li, Y. Fu, A thermo-elasto-plastic model for a fiber-metal laminated beam with interfacial damage, Applied Mathematical Modelling 39 (2015) 3317–3330.

[16] P. Wang, E. Liu, B. Zhi, An elastic-plastic model for frozen soil from micro to macro scale, Applied Mathematical Modelling 91 (2021) 125–148.

[17] Y.-N. Rao, Q. He, H.-L. Dai, A micromechanical model for effective hygro-thermo-elastic properties of fiber reinforced composites with functionally graded interphases, Applied Mathematical Modelling 92 (2021) 78–98.

[18] W. Li, N. Nguyen-Thanh, K. Zhou, Phase-field modeling of interfacial debonding in multi-phase materials via an adaptive isogeometric-meshfree approach, Engineering Fracture Mechanics 269 (2022) 108481.

[19] W. Li, N. Nguyen-Thanh, H. Du, K. Zhou, Adaptive phase-field modeling of dynamic brittle fracture in composite materials, Composite Structures 306 (2023) 116589.

[20] G. M. Vyas, S. T. Pinho, P. Robinson, Constitutive modelling of fibre-reinforced composites with unidirectional plies using a plasticity-based approach, Composites Science and Technology 71 (2011) 1068–1074.

[21] N. Nik Long, A. Khaldjigitov, U. Adambaev, On the constitutive relations for isotropic and transversely isotropic materials, Applied Mathematical Modelling 37 (2013) 7726–7740.

[22] R. J. M. Geelen, Y. Liu, T. Hu, M. R. Tupek, J. E. Dolbow, A phase-field formulation for dynamic cohesive fracture, Computer Methods in Applied Mechanics and Engineering 348 (2019) 680–711.

[23] R. Talreja, Damage development in composites: mechanisms and modelling, The Journal of strain analysis for engineering design 24 (1989) 215–222.

[24] J. D. Clayton, J. Knap, Phase field modeling of directional fracture in anisotropic polycrystals, Computational Materials Science 98 (2015) 158–169.

[25] C. Bilgen, A. Kopaničáková, R. Krause, K. Weinberg, A detailed investigation of the model influencing parameters of the phase-field fracture approach, GAMM-Mitteilungen 43 (2020) e202000005.

[26] C. Miehe, F. Welschinger, M. Hofacker, A phase field model of electromechanical fracture, Journal of the Mechanics and Physics of Solids 58 (2010) 1716–1740.

[27] E. S. Shin, K. D. Pae, Effects of hydrostatic pressure on in-plane shear properties of graphite/epoxy composites, Journal of Composite Materials 26 (1992) 828–868.

[28] G. Molnár, A. Gravouil, 2d and 3d abaqus implementation of a robust staggered phase-field solution for modeling brittle fracture, Finite Elements in Analysis and Design 130 (2017) 27–38.

[29] J. Fang, C. Wu, T. Rabczuk, C. Wu, C. Ma, G. Sun, Q. Li, Phase field fracture in elasto-plastic solids: Abaqus implementation and case studies, Theoretical and Applied Fracture Mechanics 103 (2019) 102252.

[30] U. Pillai, S. P. Triantafyllou, Y. Essa, F. M. de la Escalera, An anisotropic cohe-sive phase field model for quasi-brittle fractures in thin fibre-reinforced composites, Composite Structures 252 (2020) 112635.

[31] P. Zhang, X. Hu, T. Q. Bui, W. Yao, Phase field modeling of fracture in fiber reinforced composite laminate, International Journal of Mechanical Sciences 161-162 (2019) 105008.

[32] J. Modniks, E. Spārniņš, J. Andersons, W. Becker, Analysis of the effect of a stress raiser on the strength of a ud flax/epoxy composite in off-axis tension, Journal of Composite Materials 49 (2015) 1071–1080.

[33] Z. Z. Pan, L. W. Zhang, K. M. Liew, A phase-field framework for failure modeling of variable stiffness composite laminae, Computer Methods in Applied Mechanics and Engineering 388 (2022) 114192.

[34] Y. Zhang, J. Guo, Z. Shu, Y. Guan, A.S. Ademiloye, Fracture simulation of fiber reinforced composite panels with holes, Composite Structures, 351 (2025), 118627